



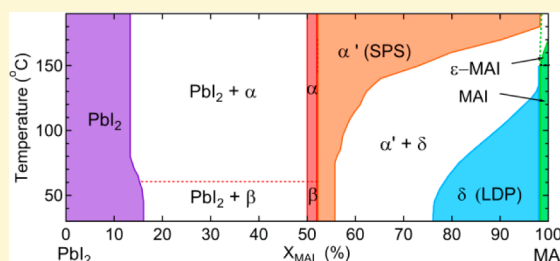
# Impact of Processing Temperature and Composition on the Formation of Methylammonium Lead Iodide Perovskites

Zhaoning Song, Suneth C. Waththage, Adam B. Phillips, Brandon L. Tompkins, Randy J. Ellingson, and Michael J. Heben\*

Wright Center for Photovoltaics Innovation and Commercialization, Department of Physics and Astronomy, School for Solar and Advanced Renewable Energy, University of Toledo, Toledo, Ohio 43606, United States

## Supporting Information

**ABSTRACT:** A delicate control of the stoichiometry, crystallographic phase, and grain structure of the photoactive material is typically required to fabricate high-performance photovoltaic (PV) devices. Organo-metal halide perovskite materials, however, exhibit a large degree of tolerance in synthesis and can be fabricated into high efficiency devices by a variety of different vacuum and solution-based processes, with a wide range of precursor ratios. This suggests that the phase field for the desired material is wider than expected or that high device efficiency may be achieved with a range of phases. Here, we investigate the structural and optical properties of the materials formed when a range of compositions of methylammonium iodide (MAI) and lead iodide ( $\text{PbI}_2$ ) were reacted at temperatures from 40 to 190 °C. The reactions were performed according to a commonly employed synthetic approach for high efficiency PV devices, and the data was analyzed to construct a pseudobinary, temperature-dependent, phase-composition processing diagram. Escape of MAI vapor at the highest temperatures (150–190 °C) enabled a  $\text{PbI}_2$  phase to persist to very high MAI concentrations, and the processing diagram was not representative of phase equilibrium in this range. Data from reactions performed with a fixed vapor pressure of MAI allowed the high temperature portion of the diagram to be corrected and a near-equilibrium phase diagram to be proposed. The perovskite phase field is wider than previously thought under both processing conditions and extended by the existence of stacked perovskite sheet phases. Several aspects of the diagrams clarify why the organo-halide perovskite materials are compatible with solution processing.



## INTRODUCTION

Over the past few years, solid-state hybrid solar cells based on perovskite organometal halides, i.e.,  $\text{CH}_3\text{NH}_3\text{PbX}_3$  ( $\text{X} = \text{I}, \text{Br}, \text{or Cl}$ ), have attracted substantial attention due to very rapid progress and photovoltaic conversion efficiencies exceeding 20%.<sup>1,2</sup> A number of approaches have been developed to fabricate perovskite solar cells with high energy conversion efficiency,<sup>3–6</sup> and the wide range of vacuum-based and solution-based approaches that are successful indicates that desired compositions and phases can be easily reached. However, despite a rapidly expanding literature that updates device performance advances, several important fundamental questions regarding the material structures and properties have not been addressed. Clearly, high-performance perovskite devices can be fabricated through the empirical optimization of various preparation pathways, but the complexity of the film formation dynamics suggest that further advances would be enabled by the development of rational synthetic guidelines. In particular, with a long-term goal of scaling-up the materials synthesis to enable fabrication of large area devices and modules, a systematic study of the impact of processing temperature and composition on the formation of organo-metal halide perovskites would be useful. Currently, such a study does not exist.

To address this need, we have performed a comprehensive study of the reaction of methylammonium iodide (MAI) and lead iodide ( $\text{PbI}_2$ ), which are the two components used in the synthesis of a prototypical perovskite material used for photovoltaics (PV), methylammonium lead iodide ( $\text{MAPbI}_3$ ). To probe the phase space, experiments were designed to examine the reaction of specific, known molar ratios of MAI to  $\text{PbI}_2$ . Fourteen different molar ratios of the components were prepared by dissolving the components in *N,N*-dimethylformamide (DMF), and films were formed by spinning aliquots of the solutions onto a 50 nm compact  $\text{TiO}_2$  layer that was prepared on soda-lime glass substrates (see Experimental Section). Each sample composition was specified in terms of the mole fraction of MAI in the mixture ( $X_{\text{MAI}}$ ), and  $X_{\text{MAI}}$  was varied between 0 and 1:

$$X_{\text{MAI}} = n_{\text{MAI}} / (n_{\text{MAI}} + n_{\text{PbI}_2})$$

Films were rapidly heated to the reaction temperature (40 to 190 °C) by placement on a preheated hot plate in a nitrogen glovebox and allowed to react for 30 min. After cooling to room

Received: March 18, 2015

Revised: May 14, 2015

Published: May 14, 2015

temperature, the properties of the films were examined by X-ray diffraction (XRD), optical absorbance (OA) spectroscopy, scanning electron microscopy (SEM), and energy-dispersive X-ray spectroscopy (EDS). The spin-coating method has led to high efficiency PV devices<sup>3,7–10</sup> and was chosen for this study to provide a homogeneous mixture of the two precursors with a well-controlled stoichiometry in a thin film form. The thin-film configuration enables rapid heat transfer and allows the phase transition study to be done on a relatively short time scale (samples were  $\sim 300$  nm thick, as determined by profilometry). Experiments confirmed that 30 min was sufficient to allow complete reaction in the thin-film samples. Longer annealing times at temperatures below  $150^\circ\text{C}$  produced no significant changes in the data, indicating near equilibrium conditions. At higher temperatures, however, MAI was lost from the film. To study the perovskite phase behavior under conditions close to equilibrium in this temperature range, additional data were collected from samples that were reacted in a sealed graphite box with excess MAI. Note that our results are expected to be similar to reactions of MAI and  $\text{PbI}_2$  in thicker films prepared by other means, including evaporation, though longer reaction times may be required.

## RESULTS AND DISCUSSION

To experimentally obtain XRD data for the phases expected to be dominant in the study, we prepared samples with  $X_{\text{MAI}} = 0$ , 0.5, and 1 and reacted the samples for 30 min at  $80^\circ\text{C}$ . Figure 1a shows the XRD data for the  $\text{PbI}_2$  ( $X_{\text{MAI}} = 0$ ), stoichiometric  $\text{MAPbI}_3$  ( $X_{\text{MAI}} = 0.5$ ), and pure MAI ( $X_{\text{MAI}} = 1$ ). The primary feature in the XRD spectra of the spin-coated  $\text{PbI}_2$  ( $X_{\text{MAI}} = 0$ ) is from the hexagonal 2H polytype,<sup>4</sup> with a strong diffraction from the (001) planes at  $2\theta = 12.6^\circ$  ( $d \approx 6.95$  Å). In contrast, the pure MAI ( $X_{\text{MAI}} = 1$ ) phase is in the tetragonal rock salt phase (space group  $P4/nmm$ ). Major features in the spectrum include diffraction peaks at  $2\theta = 9.84^\circ$ ,  $19.74^\circ$ , and  $29.79^\circ$ , which correspond to diffractions from (001), (002), and (003) planes,<sup>11</sup> respectively. The XRD spectrum of the samples prepared with  $X_{\text{MAI}} = 0.5$  should correspond to  $\text{MAPbI}_3$  perovskite. In this case, a dominant diffraction peak from (110) planes of the tetragonal  $I4/mcm$  phase ( $\beta$  phase) is observed at  $2\theta = 14.08^\circ$  ( $d \approx 6.26$  Å), with minor peaks at  $2\theta = 28.36^\circ$ ,  $31.76^\circ$ , and  $43.08^\circ$  due to (220), (310), and (330) diffractions, respectively. In this  $\beta$  phase, the  $c$  axis is slightly elongated due to the polar organic  $\text{CH}_3\text{NH}_3^+$  cation and multiple twinning in comparison to the cubic  $Pm-3m$  structure adopted by inorganic perovskites such as  $\text{CsPbI}_3$ .<sup>12</sup> Above  $60^\circ\text{C}$ , the degree of distortion in the unit cell is reduced and a second tetragonal  $P4mm$  phase ( $\alpha$  phase) becomes dominant.<sup>12–15</sup> This phase as well as the very similar cubic  $Pm-3m$  have both been referred to as the  $\alpha$  phase<sup>13–15</sup> because the  $c$ -axis distortion is very small (0.05 Å) and difficult to resolve.<sup>12</sup> The quasi-cubic  $\alpha$  and tetragonal  $\beta$  phases have very similar structures due to a small difference in energy for the configurations, and only the minor diffraction from the (211) planes at  $2\theta = 23.5^\circ$  can be used to distinguish between them.<sup>14</sup> The  $\alpha$  phase can be observed by heating samples for a long time to improve the crystallinity and rapidly reduce the temperature by quenching in an ice bath prior to XRD analysis (Supporting Information). However, for ease of experimentation, this was not done routinely. For construction of the processing diagram and proposed phase diagram (vide infra), we simply used the fact that the  $\alpha$  phase is stable above  $60^\circ\text{C}$  after verifying the literature reports for  $X_{\text{MAI}} = 0.5$ . As for the

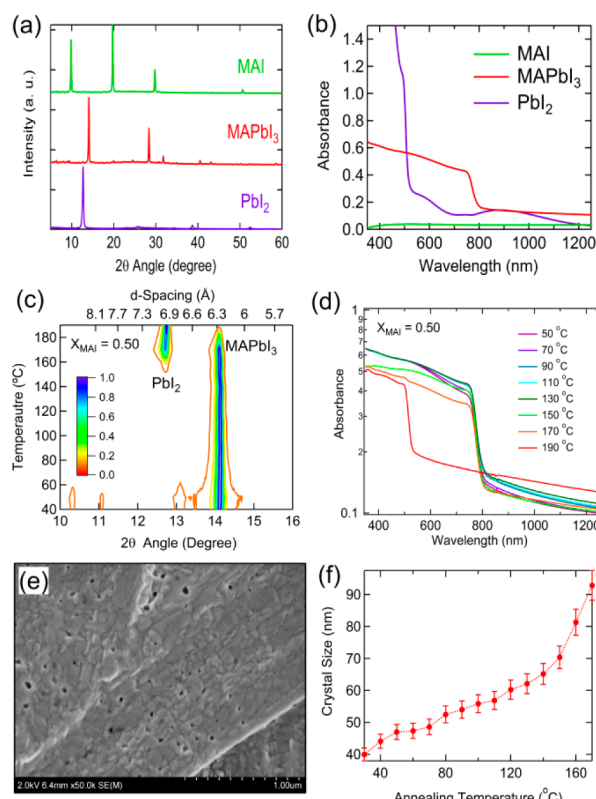


**Figure 1.** (a) X-ray diffraction and (b) optical absorbance spectra of pure phases of spin-coated  $\text{PbI}_2$ ,  $\text{MAPbI}_3$ , and MAI. (c) XRD contour plot of the room-temperature XRD mapping and (d) optical absorbance spectra of the spin-coated  $\text{MAPbI}_3$  ( $X_{\text{MAI}} = 0.5$ ) material as a function of reaction temperature. (e) SEM image of the  $X_{\text{MAI}} = 0.5$  material reacted at  $100^\circ\text{C}$ . (f) Grain size in the  $X_{\text{MAI}} = 0.5$  perovskite films as a function of reaction temperature.

reactants, MAI does form a premelting state called an ionic plastic phase at  $148^\circ\text{C}$  (Supporting Information) prior to becoming amorphous at  $170^\circ\text{C}$ ,<sup>16</sup> but this is not of significance to our study. Also, no structural phase transformations are known for pure  $\text{PbI}_2$  in the temperature range we examined.

Turning to the OA data, Figure 1b shows a relatively featureless optical absorption spectrum for pure MAI ( $X_{\text{MAI}} = 1$ ) as expected for a wide bandgap halide salt. On the other hand, the spectrum for  $\text{PbI}_2$  ( $X_{\text{MAI}} = 0$ ) shows strong absorption at wavelengths shorter than  $520$  nm consistent with the reported direct bandgap of  $\sim 2.4$  eV at room temperature.<sup>17</sup> For the material prepared at  $X_{\text{MAI}} = 0.5$ , we see the well-known band-to-band optical absorption edge at  $\sim 800$  nm ( $\sim 1.55$  eV) for  $\text{MAPbI}_3$  perovskite, with absorption that plateaus at wavelengths below  $500$  nm.<sup>18,19</sup> When the reaction temperature was increased to  $110^\circ\text{C}$ , the bandgap transition became sharper (Figure 1d). At the same time, the dominant XRD peak at  $2\theta = 14.08^\circ$  became more intense (Figure 1c), indicating a more complete conversion of the precursors and grain growth. In fact, the perovskite crystal size (estimated using the Scherrer equation) increased from  $\sim 40$  nm for films reacted at room temperature to around  $100$  nm for films formed at the higher temperatures (Figure 1e,f). However, when the reaction temperature exceeded  $150^\circ\text{C}$ ,  $\text{MAPbI}_3$  decomposed into  $\text{PbI}_2$  and MAI.<sup>12</sup> The disproportionation was complete at  $190^\circ\text{C}$  and only  $\text{PbI}_2$  was observed in both XRD and OA spectra (Figure 1c,d, respectively) due to the

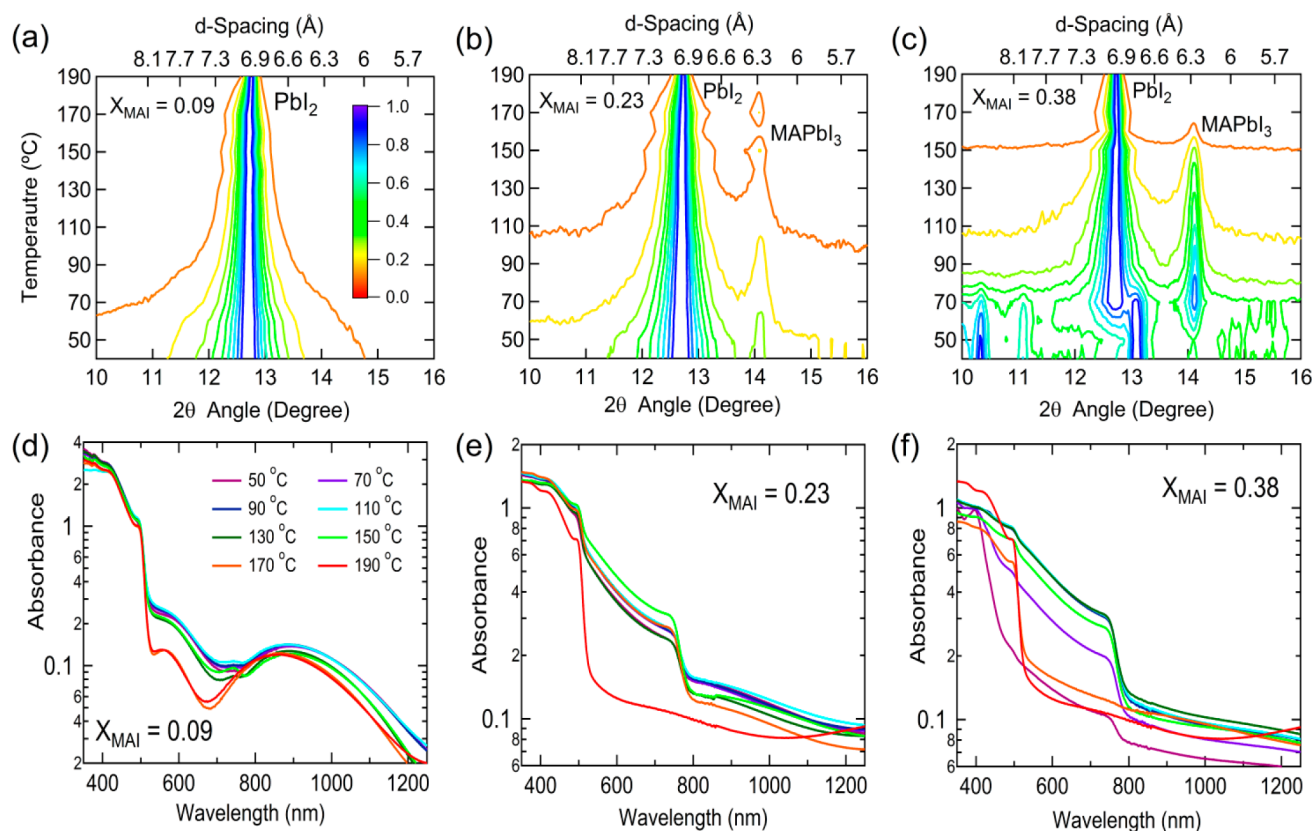


**Figure 2.** (a–c) XRD contour plots of and (d–f) optical absorbance spectra of the spin-coated nonstoichiometric MAPbI<sub>3</sub> composites with MAI percentages of 0.09, 0.23, and 0.38, respectively.

evaporation of MAI (see thermal gravimetric analysis data in the Supporting Information).

Understanding the behavior of the dominant phases assists in interpreting the XRD and OA spectra of the other compositions. Looking at the XRD data for  $X_{\text{MAI}} = 0.09$ , 0.23, and 0.38 in Figure 2a–c, respectively, it is clear that MAI-poor films ( $X_{\text{MAI}} < 0.5$ ) are comprised of either pure PbI<sub>2</sub> or mixtures of PbI<sub>2</sub> and MAPbI<sub>3</sub>. Note that diffraction features for pure MAI (Figure 1a) were never observed in the films even when the MAI concentration was high due to the lack of crystallization of a distinct MAI phase (vide infra). As  $X_{\text{MAI}}$  was increased to  $\sim 0.15$  (Supporting Information), the perovskite feature emerged as a minor phase at  $2\theta \approx 14.10^\circ$ . Below this threshold composition, e.g., at  $X_{\text{MAI}} = 0.09$ , the OA spectra are representative of PbI<sub>2</sub> at all temperatures (Figure 2d) and MAPbI<sub>3</sub> could not be resolved in the XRD data (Figure 2a). On the other hand, at  $X_{\text{MAI}} = 0.23$ , the OA spectra indicate the dominant presence of MAPbI<sub>3</sub> at all but the highest temperature (Figure 2e) even though the XRD feature at  $2\theta \approx 14.10^\circ$  is still weak (Figure 2b). Clearly, the high absorption coefficient of the perovskite causes it to dominate the long wavelength portion of the OA spectrum even when present in small amounts. As a result, determination of the phase purity of a sample solely through the use of OA measurements can be misleading. Both data sets, however, make it clear that the fraction of the MAPbI<sub>3</sub> phase in the sample decreases with increasing reaction temperature. This is due to the nucleation and growth of PbI<sub>2</sub> crystals from the amorphous precursor mixture at low temperatures and MAI vaporization at higher temperatures. More complex behavior is seen at  $X_{\text{MAI}} = 0.38$ . The XRD and OA features of the low-temperature ( $T < 70^\circ\text{C}$ )

phases have not been reported before, to our knowledge, and cannot be assigned to any reported material. However, they are likely related to the intercalation of guest MAI molecules between I–Pb–I layers, leading to structures intermediate between PbI<sub>2</sub> polytypes and perovskites.<sup>20</sup> Such intermediate structures may be similar to the MAI–PbI<sub>2</sub>–DMSO complex formed in solutions.<sup>21</sup> Overall, from the results for MAI-poor films, it is clear that PbI<sub>2</sub> cannot be completely converted into MAPbI<sub>3</sub> perovskite, as was expected.

While the phase evolution of the MAI-poor films is relatively straightforward to understand, MAI-rich films ( $X_{\text{MAI}} > 0.5$ ) exhibit more complicated structural and optical properties. This region of the phase space is perhaps most important because many preparations for high efficiency perovskite-based PV devices begin with  $X_{\text{MAI}}$  values in the range of 0.5<sup>7,8,10,22,23</sup> to 0.75.<sup>3,9,15,18,22</sup> We will first focus on the high temperature reactions since most high efficiency devices are prepared with heat treatment in the temperature range of 80–150 °C.<sup>3,7,8,15,18,22</sup>

Figure 3 shows the XRD and OA data for samples prepared with  $X_{\text{MAI}} = 0.67$ , 0.75, and 0.80. As with  $X_{\text{MAI}} = 0.5$  (Figure 1), the higher temperature reactions result in a MAPbI<sub>3</sub> phase. Here, we see that the temperature required to form the MAPbI<sub>3</sub> phase increases with increasing MAI content. For temperatures typically needed for high efficiency devices, 80–150 °C, a perovskite phase is evident and dominant until 160–170 °C, at which point the PbI<sub>2</sub> becomes dominant and MAPbI<sub>3</sub> is no longer observed. As mentioned previously, there is no XRD evidence for MAI due to the lack of order, but MAI should still be present in the quasi-liquid phase<sup>16</sup> below the melting temperature (190 °C). To examine the possibility of MAI



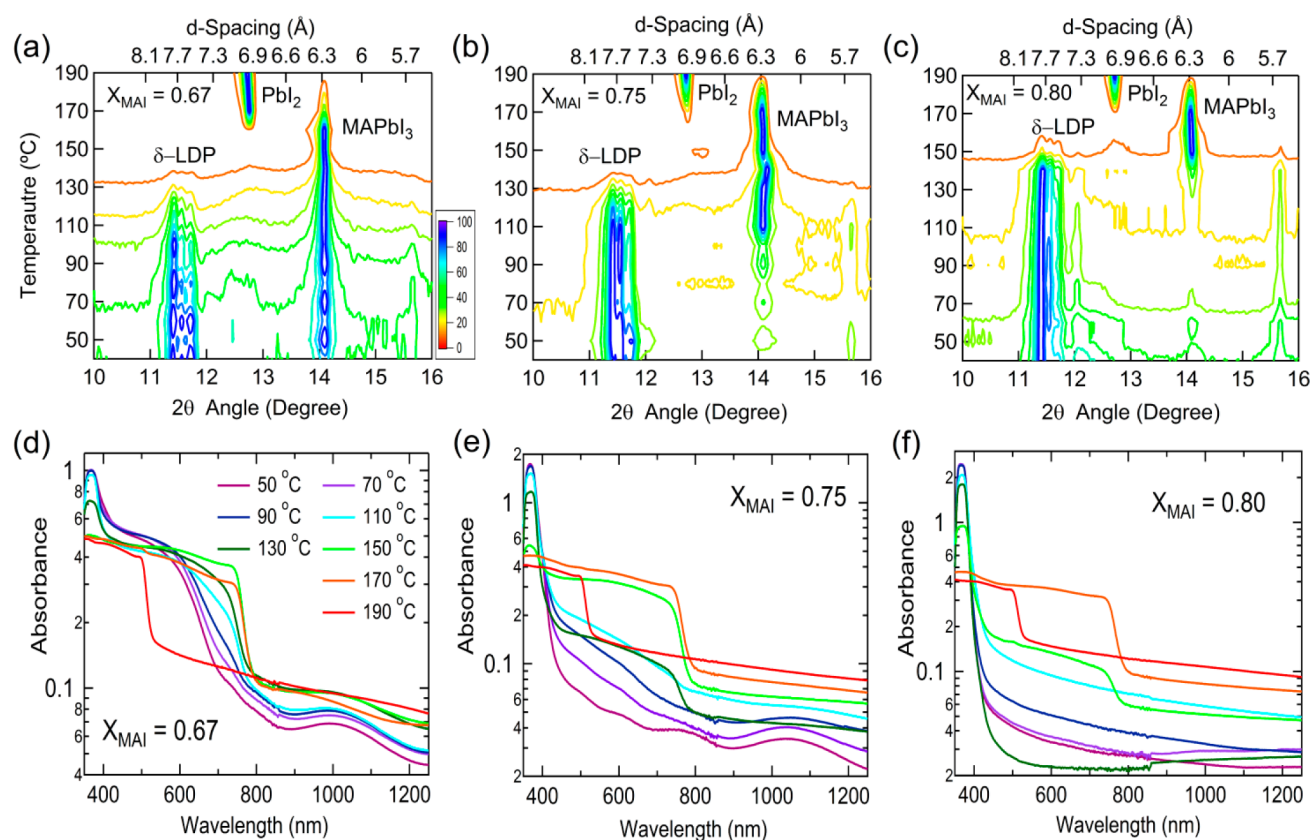


**Figure 3.** (a–c) XRD contour plots and (d–f) optical absorbance spectra of the spin-coated nonstoichiometric MAPbI<sub>3</sub> composites with MAI percentages of 0.67, 0.75, and 0.80, respectively.

evaporation, thermal gravimetric analysis of MAI powder was performed. To measure the vaporization rate, samples were held at a fixed elevated temperature in flowing N<sub>2</sub> and the weight loss was recorded as a function of time. At 150 °C, the weight loss rate was 0.002% per minute, while at the MAI melting point (190 °C) the weight loss rate was 0.032% per minute. Though the vapor pressure is evidently low at these temperatures, the high temperature portion of our phase study is clearly not in equilibrium.

The XRD (Figure 3a–c) and OA (Figure 3d–f) spectra indicate that the resultant films contain different proportions of PbI<sub>2</sub> and MAPbI<sub>3</sub>, depending on the initial composition. As will be discussed in more detail later, the data indicates that the boundary of the MAPbI<sub>3</sub> phase field persists farther than previously expected into the higher MAI content regions of the temperature/phase processing diagram. Consistently with the XRD data, EDS measurements on these samples revealed final compositions that were MAI-rich, in agreement with the precursor ratios (see the Supporting Information). Overall, these findings conflict with the recent theoretical prediction of a narrow phase field for MAPbI<sub>3</sub>.<sup>24</sup>

The existence of off-stoichiometry perovskite phases can be explained by considering the two-dimensional organic-halide perovskite materials with variable stoichiometry that have been known since the pioneering work of Mitzi.<sup>25</sup> So-called layered perovskites consist of a variable number of metal halide layers formed by corner-sharing (PbI<sub>6</sub>)<sup>4−</sup> units with associated cations that are sandwiched between intercalated organic cation bilayers. The cation bilayers keep the perovskite layers separated, retard the formation of bulk 3D perovskites, and introduce a stacking fault between adjacent metal halide

sandwiches. As  $X_{\text{MAI}}$  increases, the number of metal halide layers decreases as the density of both intercalated species and stacking faults increases. In essence, the 3D perovskite is gradually transformed into 2D layered perovskites by dissolution (Figure 4). There exists a transitional phase between 3D and 2D perovskites where the perovskite has a limited number of stacking faults and can still persist as a 3D crystal. We term this phase “stacked perovskite sheets” (SPSs). Thus, while a highly ordered perovskite phase may exist only in a narrow range close to the stoichiometric value for MAPbI<sub>3</sub>, the perovskite structures for MAI-rich films persist to values of  $X_{\text{MAI}} > 0.8$  in the form of SPSs. The crystallographic structures of perfect and stacked perovskites are not clearly distinguishable due to the same long-range periodicity of the 3D perovskite framework. However, the SPSs are indeed MAI-rich as determined by energy dispersive X-ray spectroscopy (see the Supporting Information). One might assume that defect levels in the SPS phases might lead to poor electronic quality, but a study on similar grain boundaries yielded no defect states within the band gaps.<sup>26</sup> Because of the benign nature of these defects, high efficiency devices can be fabricated in a wider composition range than would be expected.<sup>27</sup>

At the lower reaction temperatures, the MAI-rich films exhibit a distinctive XRD feature that is comprised of overlapping diffraction peaks from several components with slightly different  $d$ -spacings ( $2\theta$  between 11.3° and 11.7°). These features are dominant at the higher MAI values ( $X_{\text{MAI}} > 0.75$ , Figure 3b–c) but quenched with the appearance of the perovskite feature as the MAI concentration is decreased. These diffractions are likely due to the presence of low-dimensional perovskites (LDPs)<sup>28,29</sup> that are built up from the same

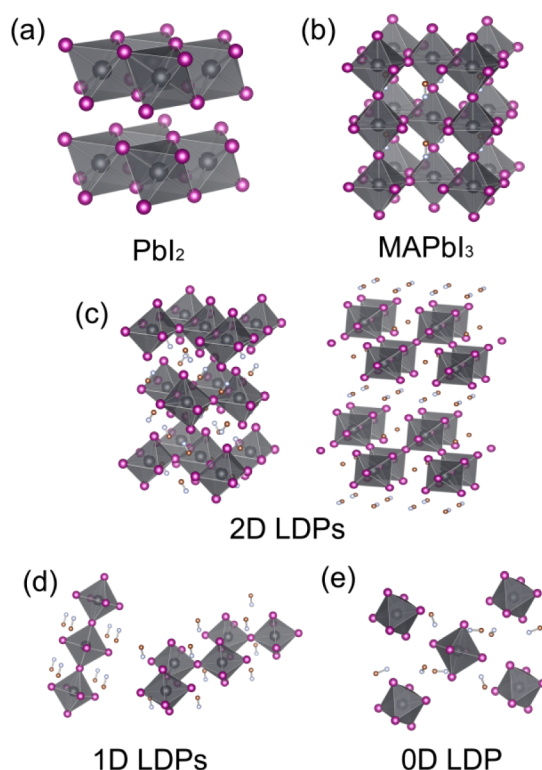


**Figure 4.** Crystal structures of (a)  $\text{PbI}_2$ , (b)  $\text{MAPbI}_3$  perovskites, (c) 2D LDPs, (d) 1D LDPs, and (e) 0D LDP.

$(\text{PbI}_6)^{4-}$  octahedral building blocks. When excess MAI is present in large concentration, the basic  $(\text{PbI}_6)^{4-}$  units exist in isolated form as zero dimensional (0D) quantum dots in an MAI matrix. As the amount of MAI is decreased, the 0D units connect and build up one-dimensional (1D) perovskite chains and 2D perovskite sheets through self-assembly, eventually leading to the assembly of 3D perovskite (Figure 4). The unique diffraction feature for LDPs arises because the structures are separated by a monolayer of intercalated  $\text{MA}^+$  cations. Thus, the spacing between the metal halide octahedra is expanded by  $\sim 1.4$  Å in comparison to the spacing in the 3D perovskite ( $d = 6.3$  Å). Consequently, the corresponding XRD peaks shift to a lower angle. There is polydispersity in structure, so the determination of the exact configurations and ratio of species is not straightforward (Supporting Information). To support the interpretation of the XRD data, note that the OA spectra of the MAI-rich composites exhibit a very strong exciton absorption centered at 370 nm, corresponding to the ground-state exciton from the 0D perovskite structure.<sup>30,31</sup> As  $X_{\text{MAI}}$  is decreased, the exciton transition is quenched while the absorption in the range of 500 to 800 nm is increased, indicating that the fraction of quantum dots is decreased as the 3D perovskites are assembled. However, evidence for perovskite quantum dots persists even at  $X_{\text{MAI}} = 0.58$  (Supporting Information), which indicates that the LDP phase region is structurally and energetically complex.

A general picture of the solid-state phase behavior for the system emerges if we consider the XRD and OA data sets for the full range of compositions and temperatures that were examined. When the MAI fraction is low ( $X_{\text{MAI}} < 0.15$ ), the only identifiable phase is  $\text{PbI}_2$ . Adding MAI results in a two-phase mixture consisting of  $\text{PbI}_2$  and perovskite  $\text{MAPbI}_3$ . The mixture tends toward  $\text{PbI}_2$  at higher temperatures, and at no

point below  $X_{\text{MAI}} = 0.5$  is the resultant material a pure perovskite. The simple fact that the perovskite signatures persist to high values of  $X_{\text{MAI}}$  ( $>0.8$ ) indicates the existence of a wide phase field. Despite the fact that EDS shows that the conventional perovskite phase ( $\alpha$ ) has an I/Pb ratio of 2.9 to 3.1, while the stacked perovskite sheet phase ( $\alpha'$ ) has an I/Pb ratio of 3.2 to 3.5 (see the Supporting Information),  $\alpha$  and  $\alpha'$  are indistinguishable by XRD and OA in our studies. The increased MAI content creates stacking faults within the perovskite and generates the SPSs. With a further increase in MAI concentration, the SPSs are broken up and solvated by  $\text{MA}^+$  cations to form thin 2D sheets, 1D chains, and 0D quantum dots (Figure 4). Interestingly, the XRD data for the MAI phase appears only when the precursor composition is very close to pure MAI ( $>99\%$ ). Evidently, even small amounts of  $\text{PbI}_2$  disrupt the crystal structure and lead to LDPs within an amorphous MAI matrix.

The findings can be compactly presented in a pseudobinary temperature/phase processing diagram (Figure 5a). To

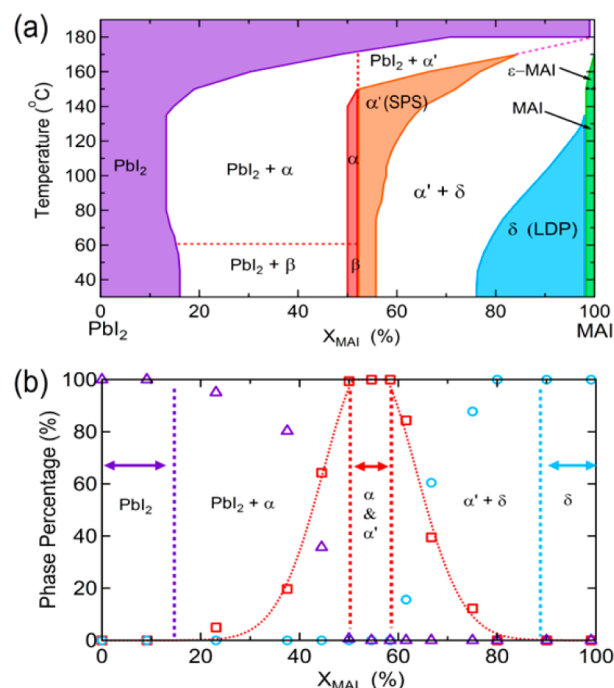


**Figure 5.** (a) Pseudobinary temperature/phase processing diagram for methylammonium lead iodide. (b) Phase percentages of  $\text{PbI}_2$  (purple triangles), perovskite (red squares), and LDP (cyan circles) as a function of MAI precursor concentration in the films reacted at 100 °C.

construct the diagram, the percentages of the phases in the films prepared at each temperature were determined by calculating the integrated XRD peak intensity ratios. For example, the amount of  $\text{MAPbI}_3$  perovskite was determined by comparing the integrated peak intensity at  $2\theta = 14.10^\circ$  to the sum of the integrated peak intensities for  $\text{PbI}_2$  ( $2\theta \sim 12.60^\circ$ ) and the low-dimensional perovskite ( $2\theta \sim 11.60^\circ$ ) peaks. The percentages of the lead iodide and LDP phases were determined in a similar way. Figure 5b is one example showing the proportions of the perovskite,  $\text{PbI}_2$ , and LDP phases in the films reacted at 100 °C as a function of the starting precursor composition. The perovskite curve was fitted by a Gaussian function to determine the pure phase region. The pure  $\text{PbI}_2$

and LDP phases are defined as the regions where the perovskite percentage was less than 0.1%. The MAI-poor side is the pure  $\text{PbI}_2$  region and the MAI-rich side belongs to the LDP phases. We then plotted the pure phase boundaries (stoichiometric limit of each pure phase) as a function of the reaction temperature (Figure 5a). The X and Y axes were swapped to correspond to a conventional view of a binary phase diagram. Finally, we assumed that the field boundaries were smooth to generate the final processing diagram.

Figure 5 can be used to understand experimental processing pathways toward the formation of perovskites, but it is not necessarily descriptive of the equilibrium phase behavior. Although the data for the low temperature ( $<150\text{ }^\circ\text{C}$ ) portion of the diagram is evidently obtained under near equilibrium conditions, the phase distribution at the higher temperatures may be affected by the evaporation of MAI. To address this possibility, several high temperature reactions were performed in a sealed graphite box that contained an equilibrium partial pressure of MAI. Interestingly, when the MAI ambient was maintained, we found that the  $\alpha'$  perovskite phase field extended fully to  $190\text{ }^\circ\text{C}$  with no evidence for  $\text{PbI}_2$ . Under these conditions, the system is much closer to equilibrium, and a phase diagram may be tentatively proposed (Figure 6a).

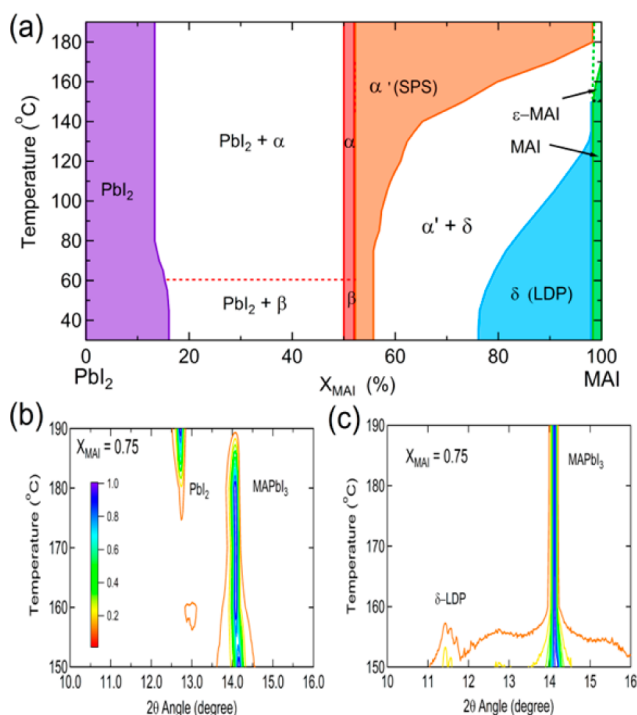


**Figure 6.** (a) Proposed phase diagram constructed with high temperature reactions carried out under a saturated MAI vapor pressure. (b, c) XRD contour plots of high temperature processed perovskites at  $X_{\text{MAI}} = 0.75$  reacted (b) on a hot plate and (c) in a sealed graphite box with a fixed MAI vapor pressure.

It is interesting to correlate our processing and proposed phase diagrams with the findings of other groups. In both diagrams, note that the perovskite phase is indeed quite wide and extended into MAI-rich regions (up to  $X_{\text{MAI}} = 0.8$ ) when the reaction temperature is high ( $>120\text{ }^\circ\text{C}$ ). This is consistent with the MAI to  $\text{PbI}_2/\text{PbCl}_2$  precursor ratios of 1:1 to 3:1 ( $X_{\text{MAI}} = 0.5$  to  $0.75$ ) that have been used in numerous solution-based syntheses.<sup>3,7–10,15,18,22,23</sup> Evidently, a relatively high

reaction temperature provides sufficient thermal energy to eliminate alkyl groups from the spaces between perovskite nanostructures<sup>28</sup> and promote the LDP to SPS phase transition. While we find good agreement at the higher temperatures, the lower temperature ( $T < 120\text{ }^\circ\text{C}$ ) MAI-rich portion of the diagram conflicts with a few materials preparations for high-efficiency perovskite devices.<sup>3,9,15,22</sup> This discrepancy may be explained by considering that these preparations were done in uncontrolled laboratory air rather than in, e.g., an inert gas environment. In these cases, it is possible that the MAI content during the film formation may have been lower than expected due to unaccounted for reactions with laboratory moisture and/or oxygen.<sup>32</sup> For example, it is well-known that halide perovskites react with water vapor at relatively low temperatures to form lead iodide as a decomposition product.<sup>33,34</sup> Accordingly, we can consider that low-temperature annealing of LDP phase samples in a moisture-containing environment can lead to a reduction in the effective MAI content during film formation/reaction. Although both low and high temperature pathways can lead to perovskites, low-temperature annealing is more widely adopted because high temperature annealing typically results in a poor surface morphology.<sup>15,35</sup> The fine details of the morphological changes during these reactions will continue to be of interest going forward.

## CONCLUSION

The formation of the perovskite  $\text{MAPbI}_3$  phase from  $\text{PbI}_2$  and MAI precursors was examined over a range of reaction temperatures and initial compositions. On the basis of the XRD, OA, TGA, and EDS results, a processing diagram was determined and a phase diagram was proposed. Both diagrams show that a pure perovskite phase occurs only in a narrow compositional space. However, an SPS phase extends the perovskite region to much higher values of  $X_{\text{MAI}}$ . We showed that the SPS phase can be formed from LDP structures by reacting at high temperatures or by decreasing the MAI concentration. The reaction pathways between the LDPs and the SPS phases provide easy routes for solution-processing via low-dimensional structures and self-assembly that allow the excellent optoelectronic properties of perovskites to be retained. Clearly,  $\text{MAPbI}_3$  perovskite is a forgiving material for polycrystalline thin film optoelectronic devices.

## EXPERIMENTAL SECTION

**Perovskite Precursor Preparation.** The perovskite methylammonium lead iodide ( $\text{CH}_3\text{NH}_3\text{PbI}_3$ ,  $\text{MAPbI}_3$ ) was prepared according to literature procedures.<sup>3,7</sup> Methylamine iodide ( $\text{CH}_3\text{NH}_3\text{PbI}$ , MAI) was first prepared by reacting hydroiodic acid (HI, 57 wt % in water, Sigma-Aldrich) with methylamine solution ( $\text{CH}_3\text{NH}_2$ , 33 wt % in ethanol, Sigma-Aldrich) under nitrogen atmosphere in a stirred ice bath for 2 h. The resulting solution was then evaporated at  $80\text{ }^\circ\text{C}$ , and the precipitate was washed three times using diethyl ether. After drying under vacuum, MAI was obtained as a white powder. The synthesized MAI and  $\text{PbI}_2$  (Sigma-Aldrich) were dissolved in anhydrous  $N,N$ -dimethylformamide at various molar ratios to prepare precursor solutions. Note that the  $\text{PbI}_2$  concentration was fixed at  $\sim 1\text{ M}$  while the MAI concentration was varied. Precursor solutions with  $\text{PbI}_2$  to MAI molar ratios of 1:0.1, 1:0.3, 1:0.6, 1:1, 1:2, 1:3, and 1:4 were prepared, corresponding to  $X_{\text{MAI}}$  values of 0.09, 0.23, 0.38, 0.50, 0.67, 0.75, and 0.8, respectively. Films were also prepared from additional precursor solutions with  $\text{PbI}_2$  to MAI molar ratios of 1:0.9, 1:1.1, 1:1.2, 1:1.3, 1:1.4, 1:5, and 1:9 and reacted at various temperatures to prove the processing/composition space.

**Substrate Preparation.** The 1 in. by 1 in. soda-lime glass substrates were sequentially cleaned with Micro-90 detergent and



deionized water in an ultrasonic bath for 30 min and dried with nitrogen gas. A compact layer of titanium dioxide ( $\text{c-TiO}_2$ ) was deposited by spin-coating titanium diisopropoxide bis(acetylacetonate) in ethanol solution (Sigma-Aldrich).<sup>4</sup> The substrates were annealed at 500 °C in air for 30 min before the deposition of perovskite thin film composites.

**Perovskite Thin Film Deposition.** To form the perovskite layer for X-ray diffraction and optical absorbance spectroscopy measurements, the precursor solutions were spin-coated on the  $\text{c-TiO}_2$  substrates at 2000 rpm in a nitrogen glovebox. After spin-coating, the films were reacted at various temperatures ranging from 30 to 190 °C with 10 °C intervals for 30 min. Standard samples were reacted on a hot plate covered with a glass Petri dish, which is a commonly employed synthetic approach for high efficiency PV devices. Additional samples were reacted in a sealed graphite box with an excess of MAI powder at temperatures ranging from 150 to 190 °C. The amount of MAI added to the graphite box was calculated to maintain a fixed MAI partial pressure. Samples were transported for characterization in a  $\text{N}_2$  sealed storage box to minimize the air exposure.

**Characterization.** X-ray diffraction spectra were collected of the prepared thin films (Rigaku Ultima III). A typical spectrum was scanned from 5° to 60° with a step size of 0.04° and a scan speed of 4° per minute in a Bragg–Brentano geometry. A fine scan covered the range of 10–16° with a step size of 0.02° and a speed of 0.50° per minute. A UV–vis spectrophotometer (PerkinElmer Lambda 1050) was used to measure the absorbance spectra in the range of 300–1200 nm. A field emission scanning electron microscope (Hitachi S-4800) was used to acquire SEM images and EDX compositional analysis. Thermogravimetric analysis (Ta Instruments Q600) was used to measure weight loss of MAI during the annealing process.

## ■ ASSOCIATED CONTENT

### ■ Supporting Information

XRD spectrum of  $\text{MAPbI}_3$ , XRD contour plots of other compositions, the evolution of XRD spectra at low temperatures, TGA of MAI and  $\text{MAPbI}_3$ , XRD spectra of the LDPs, compositional analysis and phase diagram determination methods. The Supporting Information is available free of charge on the ACS Publications website at DOI: 10.1021/acs.chemmater.5b01017.

## ■ AUTHOR INFORMATION

### Corresponding Author

\*E-mail: Michael.heben@utoledo.edu.

### Notes

The authors declare no competing financial interest.

## ■ ACKNOWLEDGMENTS

The work was supported by the Air Force Research Laboratory under Contract # FA9453-11-C-0253, the National Science Foundation under contract No CHE-1230246, and faculty start-up funds from The University of Toledo. We would like to thank Eric Ha and Elizabeth High for their input in substrate preparation and Dr. Tingting Shi for valuable discussions.

## ■ REFERENCES

- (1) Green, M. A.; Ho-Baillie, A.; Snaith, H. J. The Emergence of Perovskite Solar Cells. *Nat. Photonics* **2014**, *8*, 506–514.
- (2) NREL. *Solar Cell Efficiency Chart*. <http://www.nrel.gov>. (accessed April 2015).
- (3) Lee, M. M.; Teuscher, J.; Miyasaka, T.; Murakami, T. N.; Snaith, H. J. Efficient Hybrid Solar Cells Based on Meso-Superstructured Organometal Halide Perovskites. *Science* **2012**, *338*, 643–647.
- (4) Burschka, J.; Pellet, N.; Moon, S. J.; Humphry-Baker, R.; Gao, P.; Nazeeruddin, M. K.; Graetzel, M. Sequential Deposition as a Route to

High-Performance Perovskite-Sensitized Solar Cells. *Nature* **2013**, *499*, 316–319.

(5) Liu, M. Z.; Johnston, M. B.; Snaith, H. J. Efficient Planar Heterojunction Perovskite Solar Cells by Vapour Deposition. *Nature* **2013**, *501*, 395–398.

(6) Chen, Q.; Zhou, H.; Hong, Z.; Luo, S.; Duan, H.-S.; Wang, H.-H.; Liu, Y.; Li, G.; Yang, Y. Planar Heterojunction Perovskite Solar Cells via Vapor-Assisted Solution Process. *J. Am. Chem. Soc.* **2013**, *136*, 622–625.

(7) Kim, H. S.; Lee, C. R.; Im, J. H.; Lee, K. B.; Moehl, T.; Marchioro, A.; Moon, S. J.; Humphry-Baker, R.; Yum, J. H.; Moser, J. E.; Graetzel, M.; Park, N. G. Lead Iodide Perovskite Sensitized All-Solid-State Submicron Thin Film Mesoscopic Solar Cell with Efficiency Exceeding 9%. *Sci. Rep.* **2012**, *2*, 591.

(8) Mei, A. Y.; Li, X.; Liu, L. F.; Ku, Z. L.; Liu, T. F.; Rong, Y. G.; Xu, M.; Hu, M.; Chen, J. Z.; Yang, Y.; Graetzel, M.; Han, H. W. A Hole-Conductor-Free, Fully Printable Mesoscopic Perovskite Solar Cell with High Stability. *Science* **2014**, *345*, 295–298.

(9) Zhou, H. P.; Chen, Q.; Li, G.; Luo, S.; Song, T. B.; Duan, H. S.; Hong, Z. R.; You, J. B.; Liu, Y. S.; Yang, Y. Interface Engineering of Highly Efficient Perovskite Solar Cells. *Science* **2014**, *345*, 542–546.

(10) Nie, W. Y.; Tsai, H. H.; Asadpour, R.; Blancon, J. C.; Neukirch, A. J.; Gupta, G.; Crochet, J. J.; Chhowalla, M.; Treia, S.; Alam, M. A.; Wang, H. L.; Mohite, A. D. High-Efficiency Solution-Processed Perovskite Solar Cells with Millimeter-Scale Grains. *Science* **2015**, *347*, 522–525.

(11) Yamamuro, O.; Matsuo, T.; Suga, H.; David, W. I. F.; Ibberson, R. M.; Leadbetter, A. J. Neutron Diffraction and Calorimetric Studies of Methylammonium Iodide. *Acta Crystallogr., Sect. B* **1992**, *48*, 329–336.

(12) Stoumpos, C. C.; Malliakas, C. D.; Kanatzidis, M. G. Semiconducting Tin and Lead Iodide Perovskites with Organic Cations: Phase Transitions, High Mobilities, and Near-Infrared Photoluminescent Properties. *Inorg. Chem.* **2013**, *52*, 9019–9038.

(13) Poglitsch, A.; Weber, D. Dynamic Disorder in Methylammoniumtrihalogenoplumbates (II) Observed by Millimeter-Wave Spectroscopy. *J. Chem. Phys.* **1987**, *87*, 6373–6378.

(14) Baikie, A.; Fang, Y.; Kadro, J.; Schreyer, M.; Wei, F.; Mhaisalkar, S.; Graetzel, M.; White, T. J. Synthesis and Crystal Chemistry of the Hybrid Perovskite  $(\text{CH}_3\text{NH}_3)\text{PbI}_3$  for Solid-State Sensitized Solar Cell Applications. *J. Mater. Chem. A* **2013**, *1*, 5628–5641.

(15) Duleh, A.; Tetreault, N.; Moehl, T.; Gao, P.; Nazeeruddin, M. K.; Graetzel, M. Effect of Annealing Temperature on Film Morphology of Organic–Inorganic Hybrid Perovskite Solid-State Solar Cells. *Adv. Funct. Mater.* **2014**, *24*, 3250–3258.

(16) Ishida, H.; Ikeda, R.; Nakamura, D. Pre-Melting State of Methylammonium Iodide as Revealed by Proton Magnetic Resonance. *Phys. Status Solidi A* **1982**, *70*, K151–K154.

(17) Dugan, A. E.; Henisch, H. K. Fundamental Optical Absorption and Photo-Conduction in  $\text{PbI}_2$  Single Crystals. *J. Phys. Chem. Solids* **1967**, *28*, 1885–1890.

(18) Stranks, S. D.; Eperon, G. E.; Grancini, G.; Menelaou, C.; Alcocer, M. J. P.; Leijtens, T.; Herz, L. M.; Petrozza, A.; Snaith, H. J. Electron-Hole Diffusion Lengths Exceeding 1 Micrometer in an Organometal Trihalide Perovskite Absorber. *Science* **2013**, *342*, 341–344.

(19) Xiao, Z.; Bi, C.; Shao, Y.; Dong, Q.; Wang, Q.; Yuan, Y.; Wang, C.; Gao, Y.; Huang, J. Efficient, High Yield Perovskite Photovoltaic Devices Grown by Interdiffusion of Solution-Processed Precursor Stacking Layers. *Energy Environ. Sci.* **2014**, *7*, 2619–2623.

(20) Beckmann, P. A. A Review of Polytropy in Lead Iodide. *Cryst. Res. Technol.* **2010**, *45*, 455–460.

(21) Jeon, N. J.; Noh, J. H.; Kim, Y. C.; Yang, W. S.; Ryu, S.; Seok, S. I. Solvent Engineering for High-Performance Inorganic–Organic Hybrid Perovskite Solar Cells. *Nat. Mater.* **2014**, *13*, 897–903.

(22) Colella, S.; Mosconi, E.; Fedeli, P.; Listorti, A.; Gazzà, F.; Orlandi, F.; Ferro, P.; Besagni, T.; Rizzo, A.; Calestani, G.; Gigli, G.; De Angelis, F.; Mosca, R.  $\text{MAPb}_{(3-x)}\text{Cl}_x$  Mixed Halide Perovskite for

Hybrid Solar Cells: The Role of Chloride as Dopant on the Transport and Structural Properties. *Chem. Mater.* **2013**, *25*, 4613–4618.

(23) Laban, W. A.; Etgar, L. Depleted Hole Conductor-Free Lead Halide Iodide Heterojunction Solar Cells. *Energy Environ. Sci.* **2013**, *6*, 3249–3253.

(24) Yin, W.-J.; Shi, T.; Yan, Y. Unusual Defect Physics in  $\text{CH}_3\text{NH}_3\text{PbI}_3$  Perovskite Solar Cell Absorber. *Appl. Phys. Lett.* **2014**, *104*, 063903.

(25) Mitzi, D. B. Synthesis, Crystal Structure, and Optical and Thermal Properties of  $(\text{C}_4\text{H}_9\text{NH}_3)_2\text{MI}_4$  ( $\text{M} = \text{Ge}, \text{Sn}, \text{Pb}$ ). *Chem. Mater.* **1996**, *8*, 791–800.

(26) Yin, W. J.; Shi, T. T.; Yan, Y. F. Unique Properties of Halide Perovskites as Possible Origins of the Superior Solar Cell Performance. *Adv. Mater.* **2014**, *26*, 4653–4658.

(27) Zhang, S. B.; Wei, S. H.; Zunger, A. Stabilization of Ternary Compounds via Ordered Arrays of Defect Pairs. *Phys. Rev. Lett.* **1997**, *78*, 4059–4062.

(28) Mitzi, D. B. Solution-Processed Inorganic Semiconductors. *J. Mater. Chem.* **2004**, *14*, 2355–2365.

(29) Papavassiliou, G. C. Three- and Low-Dimensional Inorganic Semiconductors. *Prog. Solid State Chem.* **1997**, *25*, 125–270.

(30) Vincent, B. R.; Robertson, K. N.; Cameron, T. S.; Knop, O. Alkylammonium Lead Halides. Part 1. Isolated  $\text{PbI}_6^{4-}$  Ions in  $(\text{CH}_3\text{NH}_3)_4\text{PbI}_6 \cdot 2\text{H}_2\text{O}$ . *Can. J. Chem.* **1987**, *65*, 1042–1046.

(31) Hong, X.; Ishihara, T.; Nurmikko, A. V. Dielectric Confinement Effect on Excitons In  $\text{PbI}_4$ -Based Layered Semiconductors. *Phys. Rev. B* **1992**, *45*, 6961–6964.

(32) Dualeh, A.; Gao, P.; Seok, S. I.; Nazeeruddin, M. K.; Graetzel, M. Thermal Behavior of Methylammonium Lead-Trihalide Perovskite Photovoltaic Light Harvesters. *Chem. Mater.* **2014**, *26*, 6160–6164.

(33) Noh, J. H.; Im, S. H.; Heo, J. H.; Mandal, T. N.; Seok, S. I. Chemical Management for Colorful, Efficient, and Stable Inorganic–Organic Hybrid Nanostructured Solar Cells. *Nano Lett.* **2013**, *13*, 1764–1769.

(34) Frost, J. M.; Butler, K. T.; Brivio, F.; Hendon, C. H.; van Schilfgaarde, M.; Walsh, A. Atomistic Origins of High-Performance in Hybrid Halide Perovskite Solar Cells. *Nano Lett.* **2014**, *14*, 2584–2590.

(35) Eperon, G. E.; Burlakov, V. M.; Docampo, P.; Goriely, A.; Snaith, H. J. Morphological Control for High Performance, Solution-Processed Planar Heterojunction Perovskite Solar Cells. *Adv. Funct. Mater.* **2014**, *24*, 151–157.